International Communications in Heat and Mass Transfer 110 (2020) 104437

Contents lists available at ScienceDirect

International Communications in Heat and Mass Transfer

journal homepage: www.elsevier.com/locate/ichmt

Non-Newtonian behavior of an electrical and magnetizable phase change material in a filled enclosure in the presence of a non-uniform magnetic field

Mohammad Ghalambaz[a,b,*], Seyed Mohsen Hashem Zadeh[c], S.A.M. Mehryan[d], Kasra Ayoubi Ayoubloo[c], Nima Sedaghatizadeh[e]

[a] Department for Management of Science and Technology Development, Ton Duc Thang University, Ho Chi Minh City, Vietnam
[b] Faculty of Applied Sciences, Ton Duc Thang University, Ho Chi Minh City, Vietnam
[c] Department of Mechanical Engineering, Shahid Chamran University of Ahvaz, Ahvaz, Iran
[d] Young Researchers and Elite Club, Yasooj Branch, Islamic Azad University, Yasooj, Iran
[e] School of Mechanical Engineering, The University of Adelaide, Australia

ARTICLE INFO

Keywords:
Non-Newtonian phase change material (PCM)
Non-uniform magnetic field
Deformed mesh technique
Magneto hydrodynamic (MHD)
Ferro hydrodynamic (FHD)

ABSTRACT

This work aims to study the non-Newtonian behavior of a magneto- and ferro-hydrodynamic phase change material (PCM) inside a differentially heated enclosure. The enclosure is occupied with a Power-law non-Newtonian PCM, and a non-uniform magnetic field is imposed on the adjacent hot wall. The left and right of the enclosure are subjected to the high and cold temperatures, and the top and bottom of the enclosure are insulated. A deformed mesh technique along with the Stephan condition is applied to track the interface of the solid and molten regions. The impacts of the alterable parameters including the Rayleigh number ($10^4 < Ra < 10^6$), the Power-law index ($0.7 < n < 1$), the Hartman number ($0 < Ha < 250$) and the magnetic parameter ($0 < Mn_f < 7000$) on the melting front, normalized melt volume fraction (NMVF), and the Nusselt number are studied. The simulation shows that a decrease in the Power-law index can significantly increase the melting rate. In addition to this, results show that augmentation of the Hartman number and magnetic parameter weakens and enhances the NMVF, respectively.

1. Introduction

The ability to efficiently store energy is the key factor in developing a sustainable renewable energy production cycle. Thus, utilizing Thermal Energy Storage (TES) in recent years has become an appealing topic within the research communities. In fact, due to augmentation of fuel price, increasing emission of greenhouse gases and the corresponding environmental concerns, scientists' endeavors have shifted and accelerated toward improving the efficiency of harvesting energy from sustainable energy sources such as solar radiation, ocean waves, wind, and biogas [1,2]. Intermittent and discontinues nature of these resources necessitate the employment of energy storage systems as they can store energy and use it when needed [3].

In spite of the fact that diverse forms of thermal energy storage are available, latent heat thermal energy storage systems (LHTESS) are most desirable due to their compactness, high energy storage density and its ability to store heat at approximately constant temperature correspondent to the phase-transition temperature of phase change material (PCM). As such, melting and solidification of PCMs have gain augmenting consideration latterly [2,4,5]. For example, MHD phase change heat transfer of a PCM in the presence of a uniform magnetic field as a strong measure to control the melting process in a cavity has been studied theoretically by several authors [6–9]. Ghalambaz et al. [10] explored the effect of a variable magnetic field on the melting phase change heat transfer of an electrical conductive substance in a cavity.

To the best knowledge of the authors, there are just a few studies on the simultaneous effect of the FHD and MHD principles of nano-enhanced phase change materials (NEPCMs). Rostami Dibavar et al. [11] numerically surveyed phase change behaviors of aqueous NEPCMs comprising ferro-oxide nanoparticles, exposed to a non-uniform magnetic field and depicted that for non-electrical conductive magnetic nanofluids, the melting and solidification rate augments with the increment of the magnetic number. However, for electrically conductive magnetic nanofluids, increasing the Hartman number reduces the rate of the phase change process.

A comprehensive review regarding classification and application of the aforementioned materials can be found in the literature [12,13].

* Corresponding author at: Ton Duc Thang University, Ho Chi Minh City, Vietnam
E-mail address: mohammad.ghalambaz@tdtu.edu.vn (M. Ghalambaz).

https://doi.org/10.1016/j.icheatmasstransfer.2019.104437

Available online 09 December 2019

The main drawback of many PCMs is their poor thermal conductivity that reduces the melting-solidification (charging-discharging) rate and can be tackled by adding nanoparticles [14,15]. Khodadadi and Hoseinizadeh [16] studied the intensification of phase change heat transfer of PCMs through adding nanoparticles. They boosted the heat conduction of the PCM by introducing nanoparticle as additives to synthesize a nanoparticle-enhanced phase change material (NEPCM). Chamkha et al. [17] investigated the impact of using nano additives on the phase change behavior of NEPCMs in a square cavity with a hot cylinder located in its middle. Their outcomes depicted that nanoparticles volume fraction can significantly affect the interface of solid-liquid and the liquid fraction. Ghalambaz et al. [18] analyzed the effect of hybrid nanoparticles on the natural convection melting process inside a square cavity heated from the bottom and concluded that increasing the conductivity parameter and decreasing the viscosity parameter at the same time can lead to increase the liquid fraction. Sheikholeslami [19] studied solidification process of a NEPCM under the effect of a magnetic field in a porous enclosure using CuO nanoparticles and showed that by increasing the Hartmann number, total energy increases and solidification process takes lower time. In another study, Sheikholeslami [14] analyzed the solidification process of NEPCM (H_2O and CuO nanoparticles) in the presence of radiative heat transfer and a circular enclosure with metallic fins. He showed that solidification rate is amplified by increasing the length of the fins and the radiation parameter.

Dispersion of nanoparticles in the base PCM; however, affects the rheological properties of the created NEPCM as well. Hezaveh et al. [20] analyzed the rheological behavior of Fe_2O_3 magnetic nanoparticles ferrofluids in paraffin base and their magneto-viscous effects. They found that for low nanoparticles concentrations, ferrofluids behave like a Newtonian fluid, while they exhibit non-Newtonian behavior by augmentation of nanoparticles concentration. Motahar et al. [21] investigated the thermal conductivity and viscosity of n-octadecane/TiO_2 dispersions experimentally. Their outcomes showed that for low concentration of nanoparticles, the NEPCM behaved as a Newtonian fluid. While for the higher mass fraction of TiO_2 nanoparticles ($> 2\%$wt), the observed shear-thinning behavior can be acceptably modelled using Bingham Plastic model. In a similar work, Motahar et al. [22] produced a novel composite phase change material for thermal energy storage composed of dispersed mesoporous silica ($MPSiO_2$) nanoparticles in n-octadecane. They found that the viscosity of the composite presents a non-Newtonian shear thinning behavior for mass fractions of $MPSiO_2 > 3\%$ and can be modelled by the Power Law model. In addition to this, the Power-law index of discussed NEPCM decreases with the increment of the temperature and can be properly correlated between 1.0 and 0.822. Prabakaran et al. [23] experimentally studied the melting progress of fatty acid-based PCM (OM08) enhanced with the graphene nanoplatelets (GnP) in a spherical capsule and showed that by adding graphene nanoplatelets the nanocomposites shows a non-Newtonian shear thinning rheological behavior, which can be adequately modelled by Power Law model. Furthermore, the Power law index of aforementioned suspension decreases by increment of the concentration of the graphene nanoplatelets and can reach to 0.62 for 0.5% volume fraction of the GnP.

Although discussed experimental works show that the presence of the nanoparticles can induce non-Newtonian behaviors in the molten phase change materials, the literature review indicates that only Newtonian NEPCMs have studied so far. In the present paper, for the first time, the non-Newtonian rheological behavior of NEPCM is surveyed utilizing the Power Law model. Furthermore, both FHD and MHD effects are taken into consideration since the studied NEPCM (Ice/water and 8 vol% Fe_3O_4) is an electrically conductive ferrofluid.

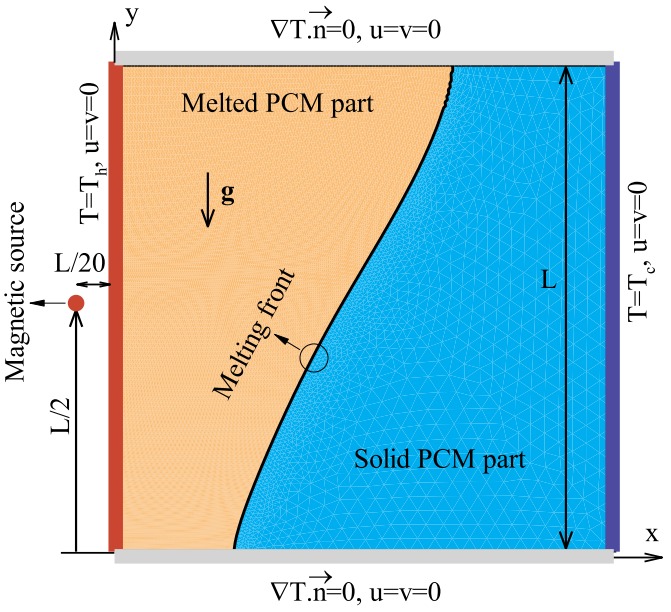

Fig. 1. Schematic representation of the problem physics.

2. Modeling

2.1. Physic of the problem

A 2D square enclosure with the dimension of L, as depicted in Fig. 1, is studied. The left of the enclosure is held at a high temperature of T_h while its right is cold with a low temperature of T_c. The remaining two bounds are perfectly insulated using an insulating substance. The coordinate origin is located at the lower left corner of the cavity and a magnetic source is placed at (x_0, y_0) out of the enclosure. The magnetic field strength radially varies as a function of distance from the source. Firstly, the phase change substance, which includes the ferromagnetic nanoparticles, is solid with the same uniform temperature. Furthermore, the homogeneous mixture model is used for the fluid-solid mixture. The molten substance behaves as a Power-law non-Newtonian suspension. Though the density of PCM varies during the melting process, it is assumed that the density variations during natural convection are not dramatic except for the buoyancy forces. Hence, the Boussinesq approximation can be utilized to estimate the buoyancy force. The thermophysical properties of the phase change substance at the solid and fluid phases, as well as the ferromagnetic nanoparticles, are provided in Table 1.

According to the previous investigations of Sheikholeslami and Vajravelu [24] and Sheikholeslami et al. [25], the intensity of the

Table 1
Thermophysical properties of ice, water, and nanoparticles.

Property [Unit]	Symbol	Ice	Water	Particles
Density (solid/liquid) [kg/m^3]	ρ	916.2	999.8	5200
Thermal expansion coefficient [1/K]	β	–	21×10^{-5}	1.3×10^{-5}
Thermal conductivity [W/m·K]	k	2.2	0.6	6
Latent heat of fusion [kJ/kg]	L_h	334	334	–
Specific heat [J/kg·K]	C_p	2050	4217	670
Dynamic viscosity [kg/m·s]	μ	–	1.79×10^{-3}	–
Volume fraction of nanoparticles	ϕ	–	–	0.08

magnetic field along the x and y axes, denoted respectively by $H_x{}^*$ and $H_y{}^*$, and the strength of the magnetic field, H^*, read as follows:

$$H_x^* = \frac{\gamma}{2\pi}\frac{(y-y_0)}{(x-x_0)^2+(y-y_0)^2} \tag{1-a}$$

$$H_y^* = -\frac{\gamma}{2\pi}\frac{(x-x_0)}{(x-x_0)^2+(y-y_0)^2} \tag{1-b}$$

$$\overrightarrow{H}^* = H_x^* i + H_y^* j,\ H^* = \sqrt{H_x^{*^2} + H_y^{*^2}} \tag{1-c}$$

2.2. Governing equations

Considering the above-explained assumptions, the governing equations describing the thermal and hydrodynamic behavior of the molten substance flow can be expressed as:

Continuity equation:

$$\rho_{nf}\nabla^*\cdot\vec{u} = 0 \tag{2}$$

$\vec{u}\,(u,v)$ in the above-written equation represents the velocity vector and ρ is the density. Subscripts *nf* denote the liquid state of the mixture, and ∇^* is the gradient vector in the *x*-*y* dimensional space.

Momentum equation:

$$\rho_{nf}\left[\frac{\partial\vec{u}}{\partial t} + (\vec{u}\cdot\nabla^*)\vec{u}\right] = \nabla^*\cdot[-pI+\tau] + \overrightarrow{F}^* \tag{3}$$

Which

$$\tau = \mu_a(\dot{\gamma})D'/2 = m_{nf}\dot{\gamma}^{n-1}D'/2 \quad \left|\ \begin{cases}\dot{\gamma} = max(\sqrt{[D']:[D']}, \dot{\gamma}_{min})\\ 2D' = (\nabla\vec{u} + (\nabla\vec{u})^{tr})\end{cases}\right. \tag{4}$$

in which μ_a is the apparent viscosity, m the consistency index, n Power-law index of the non-Newtonian fluid, I the unit matrix. The superscript of *tr* denotes the transpose of the matrix. The non-Newtonian fluids are respectively called pseudoplastic and dilatant for $n < 1$ and $n > 1$. Evidently, the fluid is Newtonian for $n = 1$. These classifications are based on the variations of an apparent viscosity as shear stress increases. For the pseudoplastic fluids, the apparent viscosity declines as the shear rate increases; however, the apparent viscosity of the dilatant fluids augments with an increment of shear rate. Also, the volume force, $\overrightarrow{F}^*$, reads as

$$\overrightarrow{F}^* = \overrightarrow{F}_L^* + \overrightarrow{F}_B^* + \overrightarrow{F}_K^* \tag{5}$$

where $\overrightarrow{F}_L^*$, the Lorentz force, is calculated as $\overrightarrow{F}_L^* = \vec{J}\times\vec{B}$, where $\vec{J}$ is the voltage field and $\vec{B}$ $(\mu_0 H_x^*, \mu_0 H_y^*)$ is the vector of magnetic induction. Furthermore, the vectors of the magnetic induction, velocity, and voltage are correlated by the following equation:

$$\vec{J} = \sigma_{nf}\vec{u}\times\vec{B} \tag{6}$$

The second component of the vlolume force, $\overrightarrow{F}_K^*$, the Kelvin force, is generated due to the gradient of the magnetic field:

$$\overrightarrow{F}_K^* = \mu_0(\overrightarrow{M}\cdot\nabla^*)\overrightarrow{H}^* \tag{7-a}$$

$$\overrightarrow{M} = -K'H^*(T-T_{Cur})i - K'H^*(T-T_{Cur})j \tag{7-b}$$

And the last one, the buoyancy force is exerted to the flow field and written as:

$$\overrightarrow{F}_B^* = \rho_{nf}\vec{g}\,\beta_{nf}(T_{nf}-T_{fu}) \tag{8}$$

in Eq. (3), t is time, p is pressure, β is thermal expansion coefficient, and $\vec{g}$ is gravity vector.

Energy balance equation for the fluid subregion:

$$(\rho C_p)_{nf}\left[\frac{\partial T_{nf}}{\partial t} + \vec{u}\cdot\nabla^* T_{nf}\right] = \nabla^*\cdot(k_{nf}\nabla^* T_{nf}) - \mu_0 T\frac{\partial\overrightarrow{M}}{\partial T}\vec{u}\cdot\nabla^*\overrightarrow{H}^* + \frac{\vec{J}\cdot\vec{J}}{\sigma_{nf}} \tag{9}$$

where μ_0 is the magnetic permeability in vacuum ($\mu_0 = 4\pi\times10^{-7}$ Tm/A). Energy equation for the solid subregion:

$$(\rho C_p)_{ns}\frac{\partial T_{ns}}{\partial t} = \nabla^*\cdot(k_{ns}\nabla^* T_{ns}) \tag{10}$$

T in the above-mentioned equation is the temperature, and C_p is the heat capacity at constant pressure. The *ns* subscript describes the properties of the combination of the solid PCM and the nanoparticles.

Applying the energy balance on the forwarding interface boundary results in the following relations:

$$u = \frac{k_{nf}\frac{\partial T_{nf}}{\partial x} - k_{ns}\frac{\partial T_{ns}}{\partial x}}{\rho_{nf}L_{h,nf}} \tag{11}$$

$$v = \frac{k_{nf}\frac{\partial T_{nf}}{\partial y} - k_{ns}\frac{\partial T_{ns}}{\partial y}}{\rho_{nf}L_{h,nf}} \tag{12}$$

where, herein, u and v are the components of the velocity of the interface boundary of the T_{fu} temperature. The governing equations are solved under the following boundary and initial conditions:

$$\forall\, x, y, t \mid t \geq 0,\ x = 0,\ 0 \leq y \leq L \Rightarrow T = T_h,\ u = v = 0 \tag{13-a}$$

$$\forall\, x, y, t \mid t \geq 0,\ x = L,\ 0 \leq y \leq L \Rightarrow T = T_c,\ u = v = 0 \tag{13-b}$$

$$\forall\, x, y, t \mid t \geq 0,\ y = 0,\ 0 \leq x \leq L \Rightarrow \frac{\partial T}{\partial y} = 0,\ u = v = 0 \tag{13-c}$$

$$\forall\, x, y, t \mid t \geq 0,\ y = L,\ 0 \leq x \leq L \Rightarrow \frac{\partial T}{\partial y} = 0,\ u = v = 0 \tag{13-d}$$

$$\forall\, x, y, t \mid t = 0,\ 0 < x < L,\ 0 < y < L \Rightarrow T = (T_h + T_c)/2,\ u = v = 0 \tag{13-e}$$

The thermo-physical properties of the fluid and solid homogenous mixture are as follows:

The density of the fluid and solid phases:

$$\rho_{nf} = (1-\phi)\rho_f + \phi\rho_{np} \tag{14-a}$$

$$\rho_{ns} = (1-\phi)\rho_s + \phi\rho_{np} \tag{14-b}$$

The heat capacity of the fluid and solid phases:

$$(\rho C_p)_{nf} = \phi(\rho C_p)_{np} + (1-\phi)(\rho C_p)_f \tag{15-a}$$

$$(\rho C_p)_{ns} = \phi(\rho C_p)_{np} + (1-\phi)(\rho C_p)_s \tag{15-b}$$

The thermal conductivity of the fluid and solid phase:

$$\frac{k_{nf}}{k_f} = \frac{(k_{np}+2k_f) - 2\phi(k_f - k_{np})}{(k_{np}+2k_f) + \phi(k_f - k_{np})} \tag{16-a}$$

$$k_{ns} = \phi k_{np} + (1-\phi)k_s \tag{16-b}$$

The consistency index of the nanofluid is:

$$m_{nf} = \frac{m_f}{(1-\phi)^{2.5}} \tag{17}$$

The thermal expansion coefficient of the fluid phase:

$$(\rho\beta)_{nf} = (1-\phi)(\rho\beta)_f + \phi(\rho\beta)_{np} \tag{18}$$

The electrical conductivity of the fluid phase

$$\sigma_{nf} = \sigma_f\left(1 + \frac{3(\sigma_{np} - \sigma_f)\phi}{(\sigma_{np} + 2\sigma_f) - (\sigma_{np} - \sigma_f)\phi}\right) \tag{19}$$

The latent heat of phase change:

$$(\rho L_h)_{nf} = (1 - \phi)(\rho L_h)_f \tag{20}$$

2.3. Non-dimensionalizing the equations

The utilized dimensionless variables transferring the equations and boundary conditions to dimensional coordinates are as below:

$$X = \frac{x}{L},\quad Y = \frac{y}{L},\quad U = \frac{uL}{\alpha_f}, V = \frac{vL}{\alpha_f},\quad \theta = \frac{T - T_{fu}}{T_h - T_{fu}}, P = \frac{L^2 p}{\rho\alpha_f^2},$$
$$H = \frac{H^*}{H_0^*},\quad H_x = \frac{H_x^*}{H_0^*},\quad H_y = \frac{H_y^*}{H_0^*}, Fo = \frac{t\alpha_f}{L^2} \tag{21}$$

where $H_0^* = \gamma/2\pi L$. Substituting the above relations for the dimensional variables in Eqs. (2), (3), (9) and (11) results in the equations below:

$$\nabla\cdot\vec{U} = 0 \tag{22}$$

$$\frac{\partial\vec{U}}{\partial Fo} + (\vec{U}\cdot\nabla)\vec{U} = \frac{\rho_f}{\rho_{nf}}\nabla\cdot\left[-PI + Pr\dot{G}^{n-1}\left[\frac{m_{nf}}{m_f}\right]\left(\nabla\vec{U} + (\nabla\vec{U})^{tr}\right)\right] + F \tag{23}$$

where

$$\dot{G} = max\left(\sqrt{[D]:[D]}, \dot{G}_{min}\right) \mid 2D = (\nabla\vec{U} + (\nabla\vec{U})^{tr}) \tag{24-a}$$

$$\vec{F} = F_X i + F_Y j \tag{24-b}$$

$$F_X = -\left[\frac{\sigma_{nf}}{\sigma_f}\frac{\rho_f}{\rho_{nf}}\right]PrHa^2H_Y^2U + \left[\frac{\sigma_{nf}}{\sigma_f}\frac{\rho_f}{\rho_{nf}}\right]PrHa^2H_XH_YV$$
$$-\frac{\rho_f}{\rho_{nf}}Mn_f\,Pr\,\theta H\frac{\partial H}{\partial X} \tag{24-c}$$

$$F_y = -\left[\frac{\sigma_{nf}}{\sigma_f}\frac{\rho_f}{\rho_{nf}}\right]PrHa^2H_X^2V + \left[\frac{\sigma_{nf}}{\sigma_f}\frac{\rho_f}{\rho_{nf}}\right]PrHa^2H_XH_YU$$
$$-\frac{\rho_f}{\rho_{nf}}Mn_f\,Pr\,\theta H\frac{\partial H}{\partial Y}\frac{\beta_{hnf}}{\beta_f} + \frac{\beta_{nf}}{\beta_f}Ra\,Pr\,\theta \tag{24-d}$$

$$\frac{\partial\theta}{\partial Fo} + (\vec{U}\cdot\nabla\theta_{nf}) = \frac{(\rho C_p)_f}{(\rho C_p)_{nf}}\left(\nabla\cdot\left(\frac{k_{nf}}{k_f}\nabla\theta_{nf}\right)\right) + Q \tag{25}$$

where

$$Q = \frac{(\rho C_p)_f}{(\rho C_p)_{nf}}\frac{\sigma_{nf}}{\sigma_f}EcHa^2\,(UH_Y - VH_X)^2 + \frac{(\rho C_p)_f}{(\rho C_p)_{nf}}Mn_f\,EcH\,(\varepsilon_1 + \theta_{nf})\left(U\frac{\partial H}{\partial X} + V\frac{\partial H}{\partial Y}\right) \tag{26}$$

$$\frac{(\rho C_p)_{ns}}{(\rho C_p)_f}\frac{\partial\theta_{ns}}{\partial Fo} = \left(\nabla\cdot\left(\frac{k_{ns}}{k_f}\nabla\theta_{ns}\right)\right) \tag{27}$$

where appeared dimensionless numbers Prandtl number *Pr*, Stephan number *Ste*, Hartman number *Ha*, Rayleigh number *Ra*, magnetic number Mn_f and Eckert number *Ec* are as follows:

Table 2
Different grid sizes for melting volume fraction.

Cases	Grid Size	Run Time
Case I	1852 Triangles	22 min
Case II	3378 Triangles	37 min
Case III	**5104 Triangles**	**51 min**
Case IV	10,873 Triangles	1 h 22 min

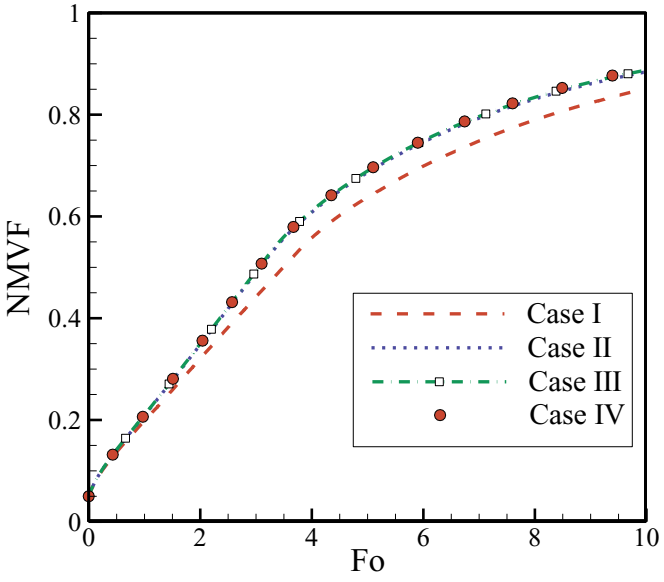

Fig. 2. Melt volume fraction for different grid size.

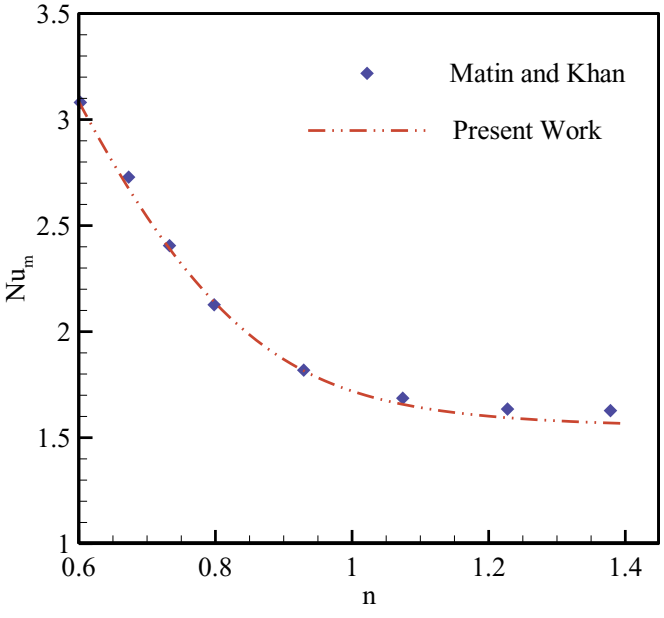

Fig. 3. Average Nusselt number against Power-law index *n* of the current study (dash-dot) and Matin and Khan [29].

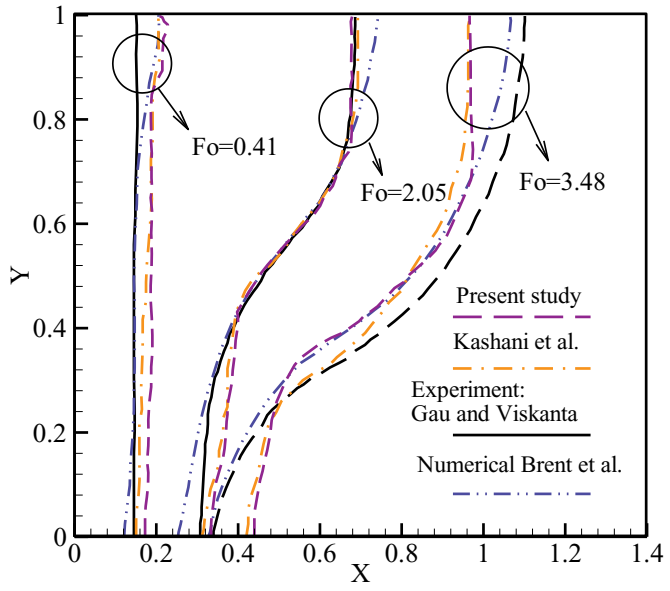

Fig. 4. Comparison between the melting front obtained by the current work and reported in [30].

$$Pr = \frac{m_f}{\rho_f \alpha_f}\left(\frac{\alpha_f}{L^2}\right)^{n-1} = \frac{m_f}{\rho_f}\frac{\alpha_f^{n-2}}{L^{2n-2}},\ Ste = \frac{C_p(T_h - T_{fu})}{L_{h,f}},\ Ha = \mu_0 H_0^* L\sqrt{\frac{\sigma_f}{m_f}},\ \varepsilon_1 = \frac{T_c}{(T_h - T_{fu})}$$
$$Ra = \frac{\rho_f g \beta_f (T_h - T_{fu}) L^{2n+1}}{m_f \alpha_f^n},\ Mn_f = \frac{\mu_0 H_0^{*2} K'(T_h - T_{fu})L}{m_f \alpha_f},\ Ec = \frac{\mu_f \alpha_f}{\rho_f C_{p,f}(T_h - T_{fu})L^2} \quad (28)$$

The velocity components of the forwarding interface boundary in the dimensionless space can be defined as follows:

$$U = \frac{1}{(1-\phi)}\left[\frac{k_{nf}}{k_f}\frac{\partial \theta_{nf}}{\partial X} - \frac{k_{ns}}{k_f}\frac{\partial \theta_{ns}}{\partial X}\right]Ste \quad (29\text{-a})$$

$$V = \frac{1}{(1-\phi)}\left[\frac{k_{nf}}{k_f}\frac{\partial \theta_{nf}}{\partial Y} - \frac{k_{ns}}{k_f}\frac{\partial \theta_{ns}}{\partial Y}\right]Ste \quad (29\text{-b})$$

The boundary and initial conditions at the dimensionless coordinates are:

$$\forall X, Y, Fo \mid Fo \geq 0, X = 0, 0 \leq Y \leq 1 \Rightarrow \theta = 1, U = V = 0 \quad (30\text{-a})$$

$$\forall X, Y, Fo \mid Fo \geq 0, X = 0, 0 \leq Y \leq 1 \Rightarrow \theta = 0, U = V = 0 \quad (30\text{-b})$$

$$\forall X, Y, Fo \mid Fo \geq 0, Y = 0, 0 \leq X \leq 1 \Rightarrow \frac{\partial \theta}{\partial Y} = 0, U = V = 0 \quad (30\text{-c})$$

$$\forall X, Y, Fo \mid Fo \geq 0, Y = 1, 0 \leq X \leq 1 \Rightarrow \frac{\partial \theta}{\partial Y} = 0, U = V = 0 \quad (30\text{-d})$$

$$\forall X, Y, Fo \mid Fo = 0, 0 < Y < 1, 0 < X < 1 \Rightarrow \theta = \theta_0 = 0.5, U = V = 0 \quad (30\text{-e})$$

Here, the parameters of interest are the volume fraction of melt and the Nusselt at the hot wall. The volume fraction of melt is normalized to the volume of the total space in the cavity. Hence, the normalized melt volume fraction is introduced as:

$$NMVF = \frac{\int_0^1 \int_0^{X_m} dXdY}{\int_0^1 \int_0^1 dXdY} \quad (31)$$

The subscript of m denotes the location of the melt-solid interface. Energy balancing of the control surface on the left wall results in the following expression:

$$h(T_h - T_c) = -k_{nf}\frac{\partial T}{\partial x}\Big)_{x=0} \quad (32)$$

The transmission of the above relation into a non-dimensional form defines another parameter of interest, namely Nusselt number Nu:

$$Nu_l = \frac{hL}{k_f} = -\frac{k_{nf}}{k_f}\frac{\partial \theta}{\partial X}\Big)_{X=0} \quad (33)$$

The average Nusselt number Nu_{avg} can be evaluated by integrating the local Nusselt number Nu_l along the hot surface:

$$Nu_{avg} = \int_o^1 Nu_l dY \quad (34)$$

3. Numerical method, grid examination and verification

The Galerkin finite element method is employed to solve the partial differential Eqs. (22), (23), (25), and (27) with the boundary constraints Eqs. (29) and (30). In the mentioned approach method, the PDEs are

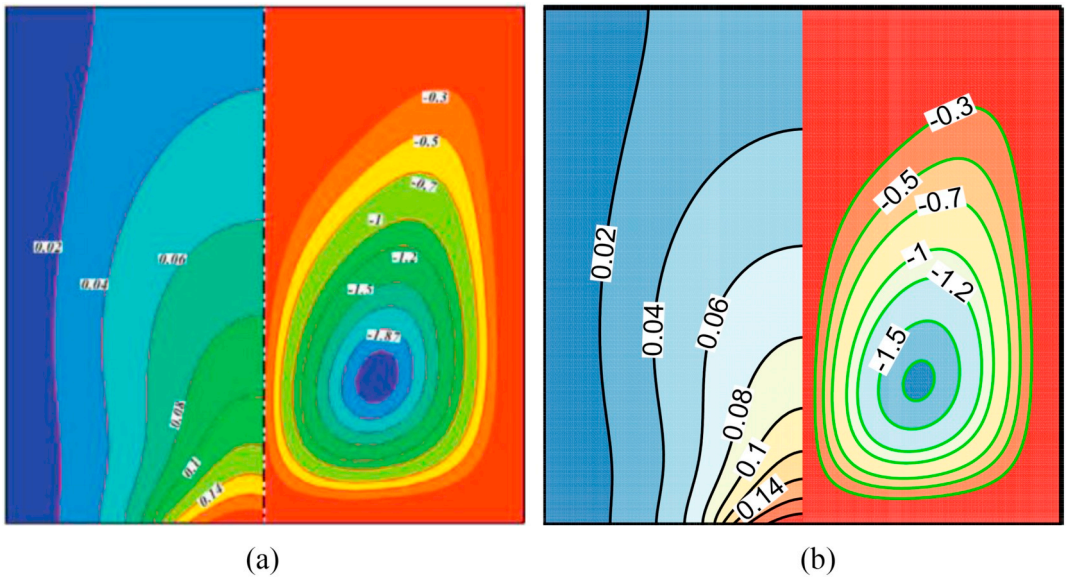

Fig. 5. Comparison between contours of temperature and streamlines of s (a): Sheikholeslami and Vajravelu [24] and (b): the current work.

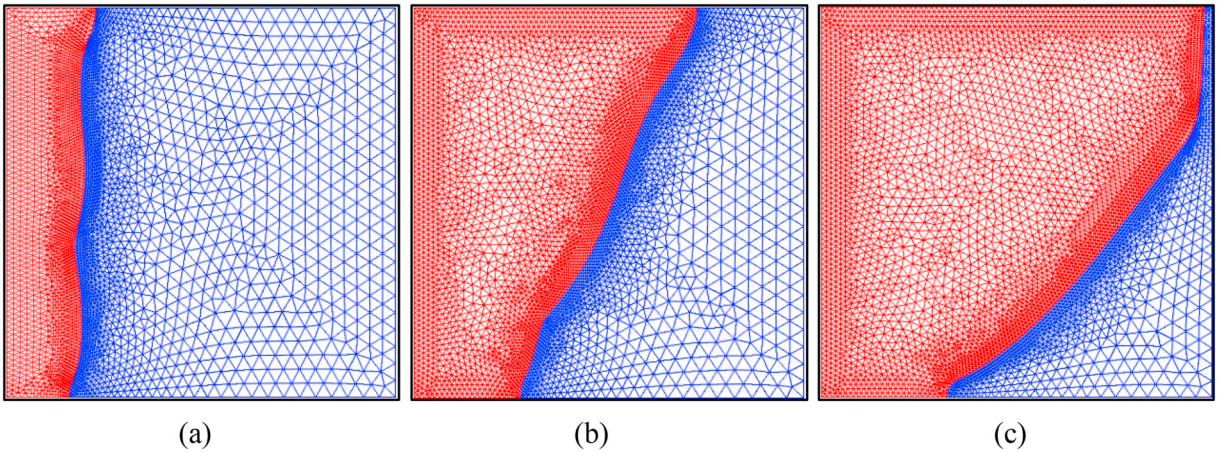

Fig. 6. Display of deformed mesh during the melting process: (a) $Fo = 1$, (b) $Fo = 5$ and (c) $Fo = 10$ (n = 0.7, $Ha = 50$, $Ra = 10^6$ and $Mn_f = 200$).

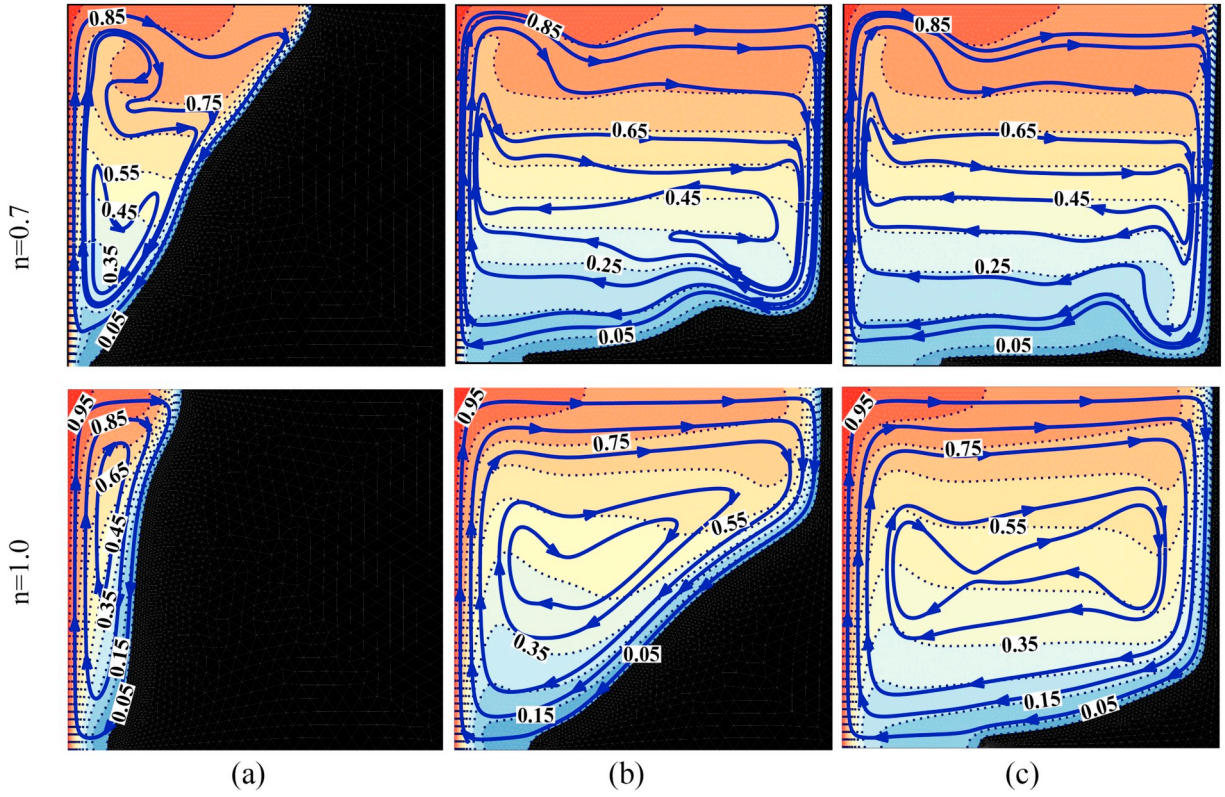

Fig. 7. Influence of the Power Law index on the isotherms (dash lines) and streamlines (solid lines) at different Fourier numbers: (a): $Fo = 1$, (b): $Fo = 5$ and (c): $Fo = 10$ ($Ha = 0$, $Ra = 10^6$ and $Mn_f = 200$).

first transferred to a new form, namely weak form. The details of the utilized numerical method can be found in [26]. The constraint for the continuity equation is introduced as a penalty parameter (γ) in the momentum equations as described by Reddy [27]. A Backward Differentiation Formula (BDF) is adopted to control the time steps and the accuracy of the solution with a free time-steps scheme [28].

To check the validity of the results of the present study, different grids are selected for grid independency check. The calculations were repeated for four types of triangular grids with sizes 1852, 3378, 5104 and 10,873 to calculate melting volume fraction for $Pr = 12.6$, $Ra = 10^6$, $Ste = 0.0126$, $Ha = 10$, $Mn_f = 200$, $\phi = 0.08$ and $n = 0.9$. Table 2 indicates melting volume fraction for different grid sizes. Melting volume Fraction of the melt for various grid resolutions is also illustrated in Fig. 2. As seen, the case III depicts admissible accuracy and thus the results of the present study are carried out using the grid size 5104 triangles.

The correctness and accuracy of the numerical outcomes can be verified and validated through the other numerical and experimental results, respectively, reported in [24,29,30]. To verify the natural convection of a non-Newtonian Power-law fluid in an enclosure, the study of Matin and Khan [29] is re-stimulated through the utilized code in the present study. Matin and Khan [29] studied the free heat transfer of a non-Newtonian Power-law fluid in annuli of the horizontal cylinders with the hot and cold temperatures at the inner and outer cylinders. For a case of non-Newtonian fluid with $Pr = 10$ and $Ra = 10^3$, a comparison between the average Nusselt numbers of the present study and those of [29] is displayed in Fig. 3 for different values of the Power-law index. As shown, the results are in excellent agreement.

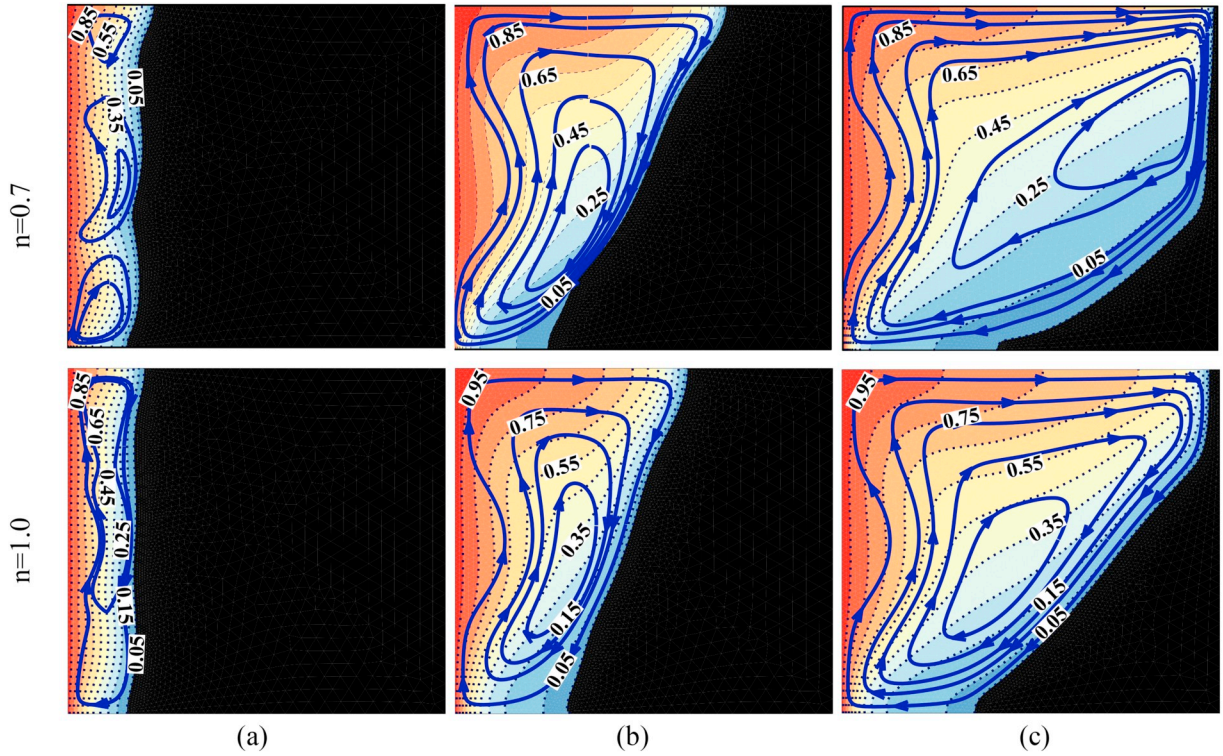

Fig. 8. Influence of the Power Law index on the isotherms (dash lines) and streamlines (solid lines) at different Fourier numbers (Ha = 50, Ra = 10^6, and Mn_f = 200).

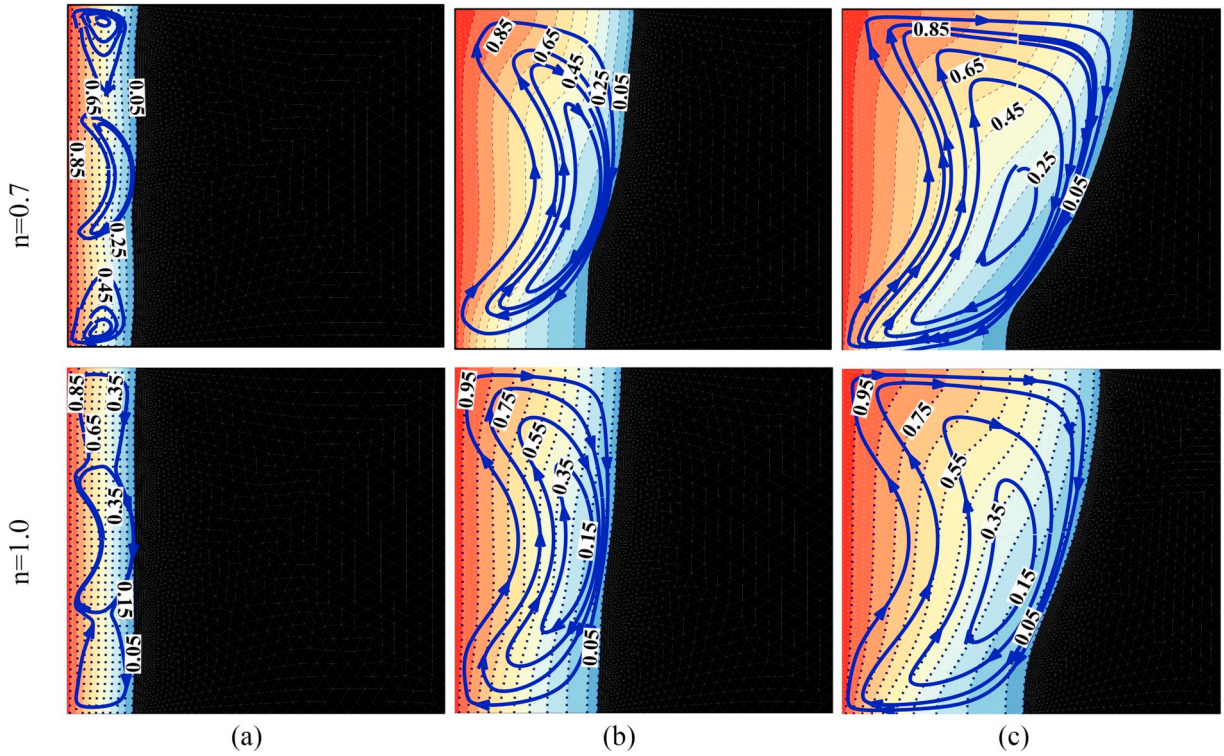

Fig. 9. Influence of the Power Law index on the isotherms (dash lines) and streamlines (solid lines) at different Fourier numbers: (a): Fo = 1, (b): Fo = 5 and (c): Fo = 10 (Ha = 150, Ra = 10^6 and Mn_f = 200).

For validation and verification of the melting process, comparisons between the melting fronts obtained in the present study and those presented in [30] are conducted, as depicted in Fig. 4. The problem physics studied in [30] included a square cavity with the horizontal insulated walls, while a constant temperature difference was considered for the sidewalls of the cavity. The pure gallium was selected as the Newtonian phase change substance. The dimensionless parameters based on the thermo-physical properties of the PCM, the thermal

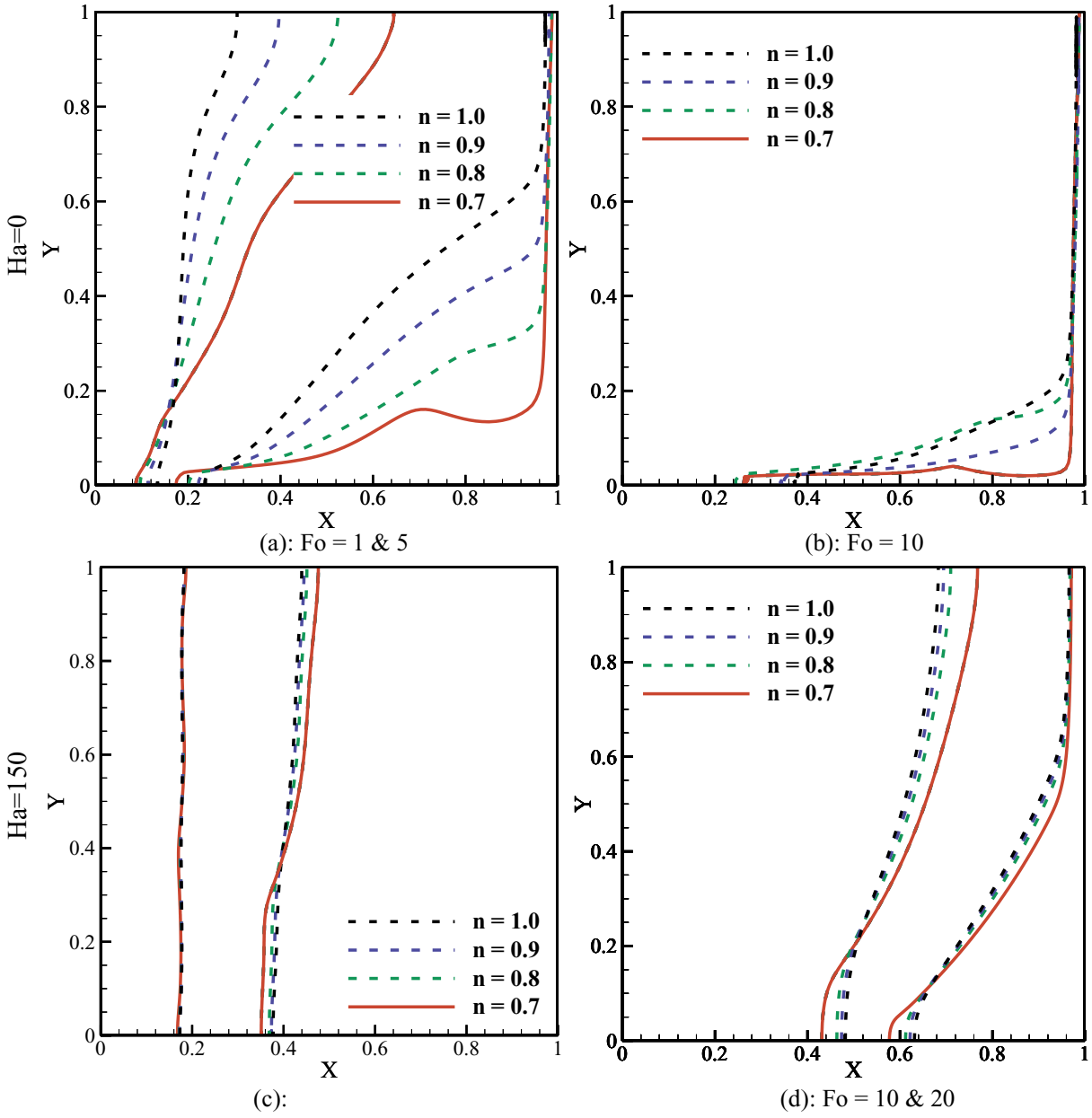

Fig. 10. The melting interface for various n-index, Hartman, and Fourier numbers ($Ra = 10^6$ and $Mn_f = 200$).

boundary conditions, and the geometrical characteristics were such that $Pr = 0.0216$, $Ra = 6 \times 10^5$, and $Ste = 0.039$. As shown in Fig. 4, the results of the current work are in good agreement with Gau and Viskanta [30].

At the last verification, the natural convection heat transfer of a magnetic nanofluid inside an enclosure is compared against the study conducted by Sheikholeslami and Vajravelu [24]. The bottom of the enclosure was partially subjected to constant heat flux, while the top wall maintained at the cold temperature. The other walls of the enclosure were perfectly insulated. A non-uniform magnetic field is imposed on the enclosure. The constant parameters for this evaluation are $Pr = 6.8$, $Ha = 10$, $\phi = 0.04$, $Ra = 10^5$ and $Mn_f = 0$. The comparison is plotted in Fig. 5, which shows that there is a desirable agreement between the results.

4. Results and discussion

This portion deals with the results obtained by modeling of the natural convection of a non-Newtonian PCM under the influence of a non-uniform magnetic field. According to the data inserted in Table 1, $Pr = 12.6$, $Ste = 0.0126$, and $\phi = 0.08$ are selected as the fixed parameters. The heat generation term, i.e. Q, is negligible since the order of Eckert number is $O = O(10^{-17})$. Moreover, the effect of other parameters including Rayleigh number $Ra = 10^3$–10^6, Hartman number $Ha = 0$–250, Magnetic number $Mn_f = 0$–7000, and Power-law index $n = 0.7$–1.0 is investigated. The technique of re-meshing during the melting process is employed to satisfy the precision of the results. Fig. 6 shows the deformable grid pattern for three non-dimensional-time during the melting process. As shown, the grid pattern moves and changes by various Fourier number.

Figs. 7–9 illustrate the influence of the Power-law index and the Hartman number on the patterns of isotherms and streamlines, at different Fourier numbers. As seen, the melting process proceeds by increasing the Fourier number, and the melted liquid region develops. The isotherms at primary stages of the process are approximately vertical, indicating that the melting of the NEPCM is mainly controlled by

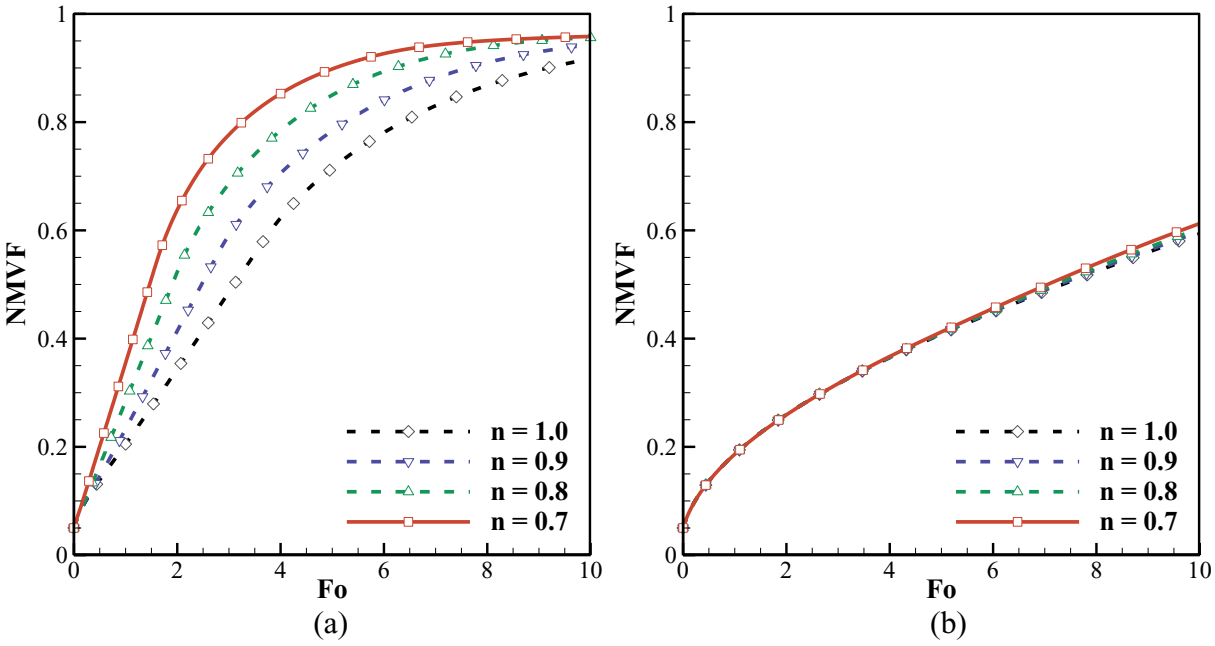

Fig. 11. The effect of n-index on the normalized melt volume fraction: (a): $Ha = 0$ and (b): $Ha = 150$ ($Mn_f = 200$ and $Ra = 10^6$).

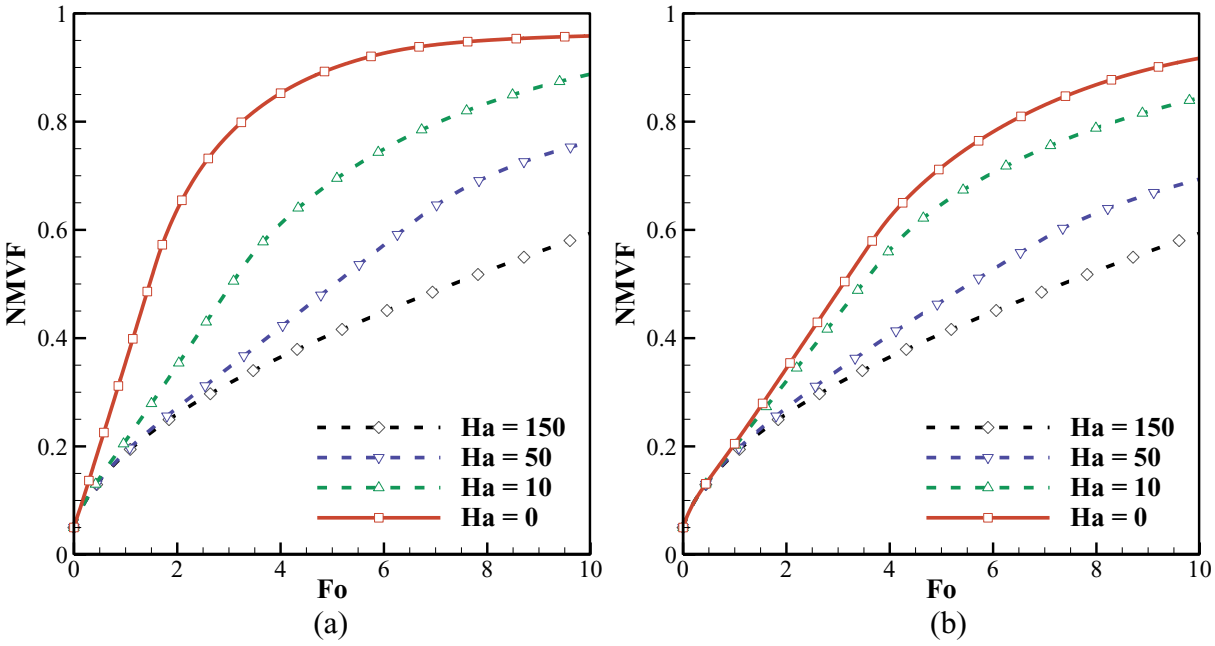

Fig. 12. The normalized melt volume fraction variation with the Hartman number: (a): $n = 0.7$ and (b): $n = 1.0$ ($Ra = 10^6$ and $M_{nf} = 200$).

the conduction mode, while the convection mechanism becomes dominant as the liquid fraction in the cavity increases. It is evident that the transition to the non-Newtonian fluid intensifies the melting rate. This is due to the reduction in the apparent viscosity of shear-thinning fluids compared to Newtonian fluids, which leads to the increase in convection strength and consequently the melting rate. As can be seen from Figs. 7–9, both melting time and the molten fraction depend strongly on the strength of the exerted magnetic field. Boosting Lorentz force imposes extra resistance on the motion of the fluids and thus reduces the rate of the convection heat transfer. As a result, the melting rate is highly affected as the Hartman number increases.

To investigate the influence of the Power Law index and the Hartman number more precisely, the melting front at different values of *Ha* and n indexes are depicted in Fig. 10 for various non-dimensional time. It is evident that the influence of the *n* index is more enormous in the absence of the Lorentz force (Fig. 10a and b). Increasing the Hartman number, as discussed before, slows the melting process. In addition to this, the melting front remains almost vertical in the case of high Hartman numbers ($Ha = 150$) even in the last stages of the melting ($Fo = 10, 20$), indicating the existence of an equilibrium between the conduction and convection heat transfer mechanisms.

The influence of the Power Law index on the NMVF for two values of Hartman number ($Ha = 0$ and 150) is depicted in Fig. 11. It is obvious that a larger melted fraction can be achieved as the rheological behavior of the material transitions from the Newtonian to the shear-thinning fluid. In fact, due to the apparent viscosity reduction, the friction decreases, and the fluid flows more easily and boosts the melting rate.

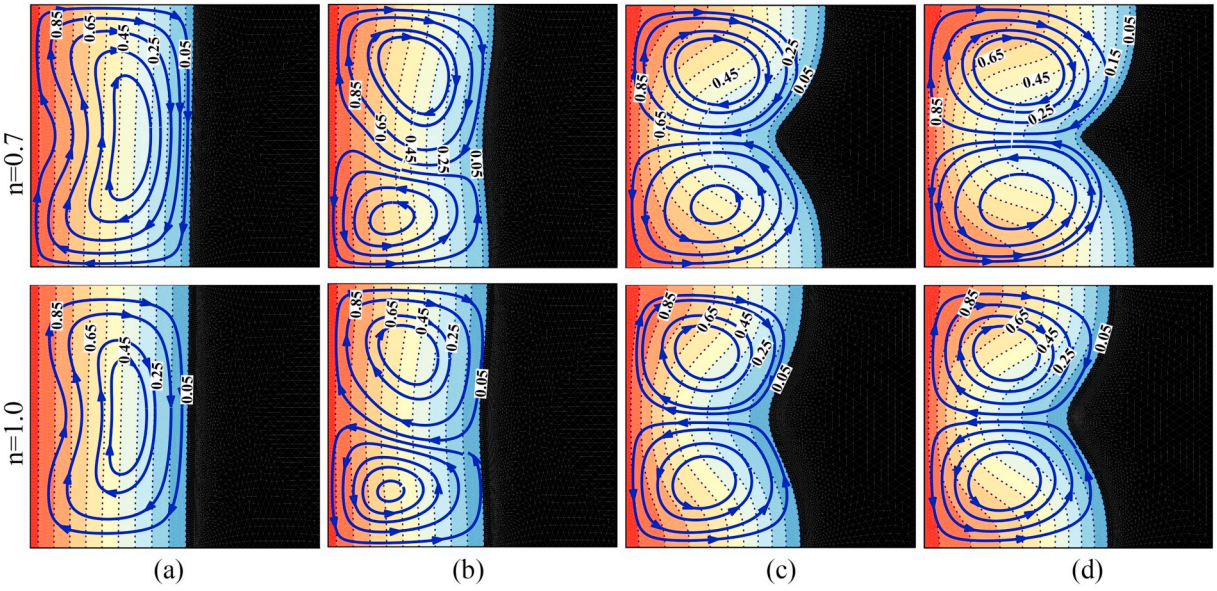

Fig. 13. Isotherms (dash lines) and streamlines (solid lines) for various values of the Power-law index and magnetic number: (a): Mnf = 0, (b): Mnf = 1000, (c): Mnf = 5000 and (d): Mnf = 7000 ($Ra = 10^3$, $Ha = 10$ and $Fo = 10$).

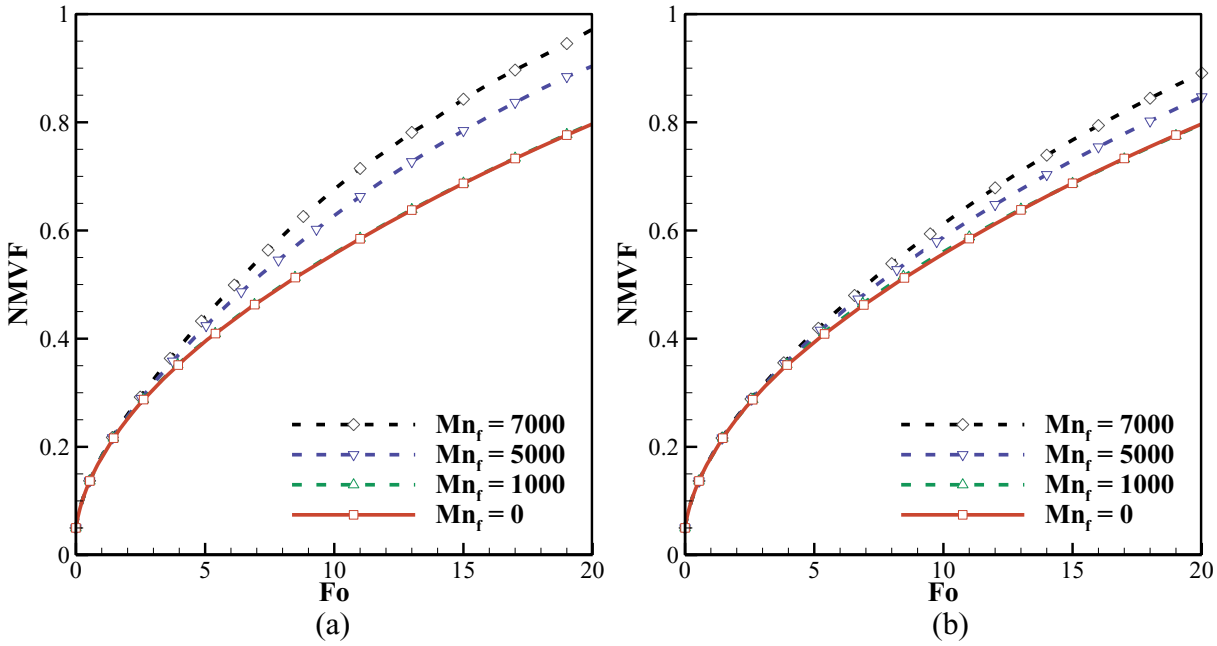

Fig. 14. The dependence of the normalized melt volume fraction on the Mn_f: (a): n = 0.7 and (b): n = 1.0 ($Ha = 10$ and $Ra = 10^4$).

The time growth of the normalized melted volume fraction and its dependency on the *Ha* is shown in Fig. 12. Regardless of the strength of the exerted Lorentz force, the initial stage of the graphs coincides with each other, specifying the dominance of the conduction heat transfer. The conduction stage of the melting; however, decreases with the Power-law index reduction ($0 \le Fo \le 0.4$ for $n = 0.7$ and $0 \le Fo \le 1.0$ for Newtonian fluid) as it consequently boosts the convection strength. It is evident from Fig. 12a that the Hartman number affect the melting rate to a greater extent when the fluid is non-Newtonian. It can be described by the fact that the velocity gradients of the shear-thinning fluid are higher than the Newtonian one. Moreover, as the Lorentz force depends on both magnetic field and the magnitude of the velocity field (See Eq. (24)), its influence on the melting rate is more intensive.

The effect of the magnetic number on the isotherms and streamlines for different rheological behaviors of the fluid ($n = 1.0$ and $n = 0.7$) are depicted in Fig. 13. The results are shown for the case $Ra = 10^3$ as the effect of the Kelvin force is more pronounced at low values of the Rayleigh number. The Kelvin force shows to affect the flow pattern strongly as a single vortex is formed when the FHD principle is not taken into account ($Mn_f = 0$). Increasing magnetic parameter ($Mn_f = 1000$) leads to the creation of two separate vortices rotating in opposite directions. A symmetric flow field can be found for the higher values of the Kelvin force, which shows a force balance between the gravity and Kelvin forces. In addition to this, and as discussed before, the melted fraction for the shear-thinning fluid ($n = 0.7$) is higher due to the declined apparent viscosity. It should be noted that in contrast with the Lorentz force, the Kelvin force is independent of the velocity field and thus its impact on the flow field is subjected to the rheological behavior of the fluid.

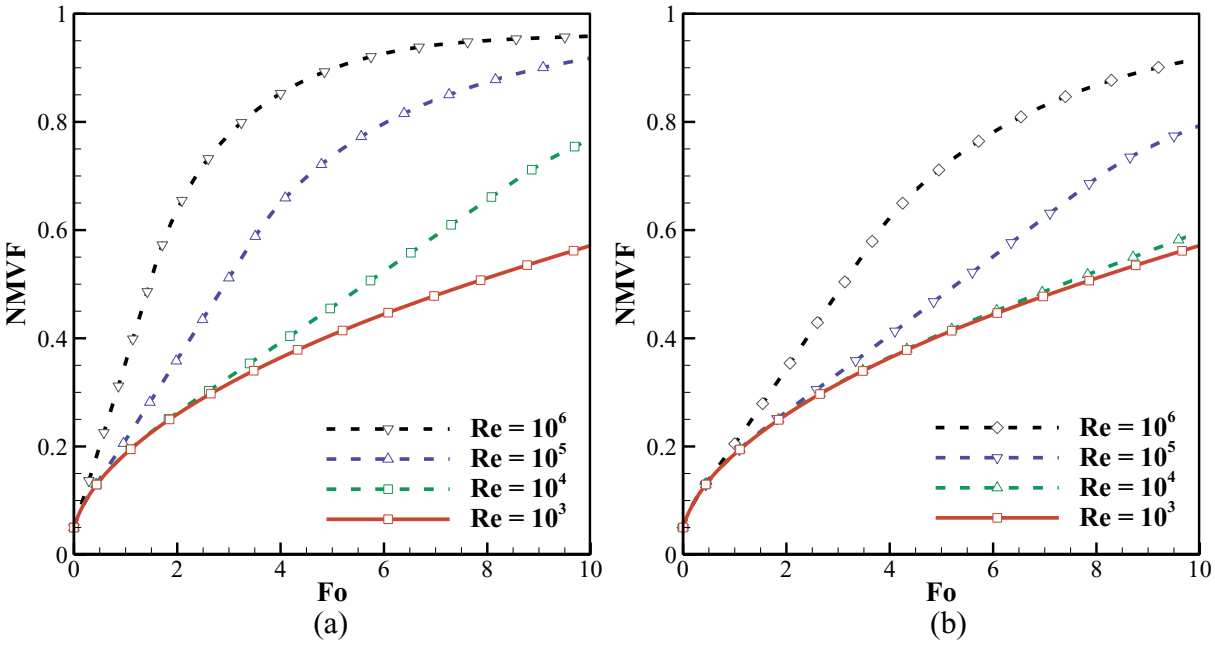

Fig. 15. The effect of the Rayleigh number on the normalized melt volume fraction: (a): n = 0.7 and (b): n = 1.0 (Mn_f = 200 and Ha = 10).

The dependence of the normalized melted volume fraction of the studied fluid on the magnetic parameter for two rheological behaviors (n = 0.7 and 1.0) is shown in Fig. 14. It is evident that increasing the Kelvin force results in a significant reduction in the required time for the melting process of the NEPCM. Moreover, the melting rate for the case n = 0.7 is higher because of the superposition of the Kelvin force and the increment of the convection strength.

The influence of the Rayleigh number on the NMVF for two cases of the fluids, namely the Newtonian and shear-thinning fluid (n = 7) is illustrated in Fig. 15. Rayleigh number represent the buoyancy force and thus the melting time process decreases significantly by the increase of Rayleigh number. The Rayleigh number also shows to reduce the conduction melting stage as the graphs coincide sections (either Fig. 15a and b) decrease when the Ra increases. Again, the increment of the melting rate is more remarkable for the case of n = 0.7 due to the lower viscosity and thus the friction of the fluid.

The alteration of the average Nusselt number with the (a) magnetic parameter and (b) Hartman number is depicted in Fig. 16. Increasing the Mn_f slightly boosts the flow strength and thus increases the rate of transferred heat from the hot wall to some extent (Fig. 16a). In addition to this, due to the increment of the fluid flow caused by the shear-thinning behavior of the NEPCM, the Nusselt number increases as the Power Law index decreases. In other words, the rate of transferred heat can be intensified up to 50% when the Power Law index is 0.7. Fig. 16b shows that the Nu_{avg} declines as the values of the Ha increases. As discussed before, this relates to the reduction of the convection strength

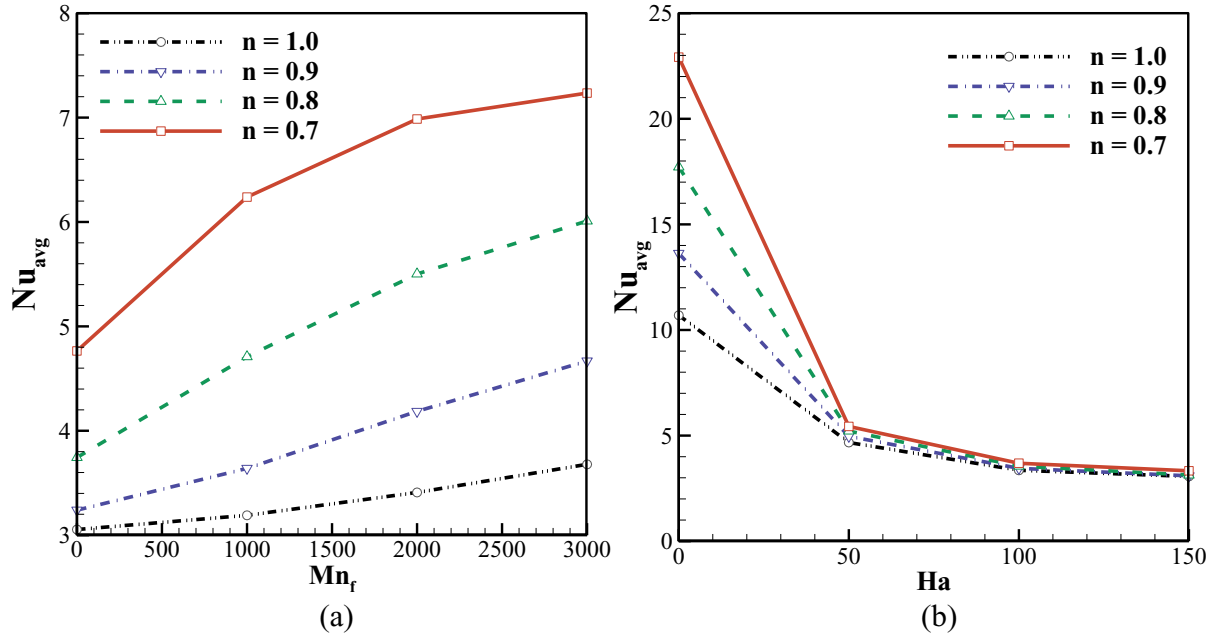

Fig. 16. Variation of the Nusselt number with: (a): Mn_f (Ha = 0) and (b): Ha (Mn_f = 200), (Fo = 5 and Ra = 10^6).

of the fluid. Moreover, the dependence of the Nusselt number to the Power-law index decrease as the Hartman number increases, which is explained by the dominance of the Lorentz force in the flow field.

5. Conclusion

The rheological behavior of a nano-enhanced phase change material (Ice/water and 8 vol% Fe_3O_4) is studied numerically. The Finite element Galerkin method is employed to solve the non-dimensional governing equations. As well as this, the deformed mesh technique is used to capture the advancement of the melting front. Both Kelvin and Lorentz forces are taken into account as source terms in the momentum and energy equations since the NEPCM is considered to behave as an electro-conductive ferrofluid. The Power law model is utilized for the shear-thinning behavior of the fluid. The summary of the outcomes are as follows:

1. The Power-law index reduces the melting process time strongly in the absence of the magnetic field. This is due to the fact that the apparent viscosity declines as the *n* index decreases and thus reduces the friction of the fluid.
2. By applying the magnetic field, the influence of the n index on the melting time declines as the flow field entirely affects by the Lorentz force.
3. The raise of the Hartman number slows down the melting process by imposing extra resistance to the fluid motion.
4. The magnetic parameter reduces the required time for the melting process as it boosts the convection strength of the flow field.
5. The average Nusselt number is intensified with the increment of the *n* index and magnetic parameter and declines as the Hartman number increases. The heat transfer can be improved by up to 50% when the Power Law index is 0.7.

References

[1] I. Sarbu, C. Sebarchievici, A comprehensive review of thermal energy storage, Sustainability 10 (1) (2018) 191.
[2] A.F. Regin, S.C. Solanki, J.S. Saini, Heat transfer characteristics of thermal energy storage system using PCM capsules: a review, Renew. Sust. Energ. Rev. 12 (9) (2008) 2438–2458.
[3] Y. Menni, A. Azzi, A.J. Chamkha, A review of solar energy collectors: models and applications, J. Appli. Computati. Mech. 4 (4) (2018) 375–401.
[4] M.M.A. Khan, N.I. Ibrahim, I. Mahbubul, H.M. Ali, R. Saidur, F.A. Al-Sulaiman, Evaluation of solar collector designs with integrated latent heat thermal energy storage: a review, Sol. Energy 166 (2018) 334–350.
[5] A. Sharma, V.V. Tyagi, C.R. Chen, D. Buddhi, Review on thermal energy storage with phase change materials and applications, Renew. Sust. Energ. Rev. 13 (2) (2009) 318–345.
[6] M. Ghalambaz, A. Doostanidezfuli, H. Zargartalebi, A.J. Chamkha, MHD phase change heat transfer in an inclined enclosure: effect of a magnetic field and cavity inclination, Num. Heat Transfer A Appl. 71 (1) (2017) 91–109.
[7] A. Doostani, M. Ghalambaz, A.J. Chamkha, MHD natural convection phase-change heat transfer in a cavity: analysis of the magnetic field effect, J. Braz. Soc. Mech. Sci. Eng. 39 (7) (2017) 2831–2846.
[8] R.Y. Farsani, A. Raisi, A.A. Nadooshan, S. Vanapalli, The effect of a magnetic field on the melting of gallium in a rectangular cavity, Heat Transfer Eng. 40 (1–2) (2019) 53–65.
[9] M. Sheikholeslami, H.B. Rokni, Melting heat transfer influence on nanofluid flow inside a cavity in existence of magnetic field, Int. J. Heat Mass Transf. 114 (2017) 517–526.
[10] M. Ghalambaz, S.M.H. Zadeh, S. Mehryan, I. Pop, D. Wen, Analysis of melting behavior of PCMs in a cavity subject to a non-uniform magnetic field using a moving grid technique, Appl. Math. Model. 77 (2020) 1936–1953.
[11] M. Rostami Dibavar, M. Mohammadpourfard, F. Mohseni, S. Zeinali Heris, Numerical study on the effect of non-uniform magnetic fields on melting and solidification characteristics of NEPCMs in an annulus enclosure, Energy Convers. Manag. 171 (2018) 879–889.
[12] L.F. Cabeza, A. Castell, C. Barreneche, A. de Gracia, A.I. Fernández, Materials used as PCM in thermal energy storage in buildings: a review, Renew. Sust. Energ. Rev. 15 (3) (2011) 1675–1695.
[13] B. Zalba, J.M. Marín, L.F. Cabeza, H. Mehling, Review on thermal energy storage with phase change: materials, heat transfer analysis and applications, Appl. Therm. Eng. 23 (3) (2003) 251–283.
[14] M. Sheikholeslami, Numerical modeling of nano enhanced PCM solidification in an enclosure with metallic fin, J. Mol. Liq. 259 (2018) 424–438.
[15] A. Nematpour Keshteli, M. Sheikholeslami, Nanoparticle enhanced PCM applications for intensification of thermal performance in building: a review, J. Mol. Liq. 274 (2019) 516–533.
[16] J.M. Khodadadi, S.F. Hosseinizadeh, Nanoparticle-enhanced phase change materials (NEPCM) with great potential for improved thermal energy storage, Int. Commun. Heat Mass Transfer 34 (5) (2007) 534–543.
[17] A.J. Chamkha, A. Doostanidezfuli, E. Izadpanahi, M. Ghalambaz, Phase-change heat transfer of single/hybrid nanoparticles-enhanced phase-change materials over a heated horizontal cylinder confined in a square cavity, Adv. Powder Technol. 28 (2) (2017) 385–397.
[18] M. Ghalambaz, A. Doostani, E. Izadpanahi, A.J. Chamkha, Phase-change heat transfer in a cavity heated from below: the effect of utilizing single or hybrid nanoparticles as additives, J. Taiwan Inst. Chem. Eng. 72 (2017) 104–115.
[19] M. Sheikholeslami, Solidification of NEPCM under the effect of magnetic field in a porous thermal energy storage enclosure using CuO nanoparticles, J. Mol. Liq. 263 (2018) 303–315.
[20] H. Hezaveh, A. Fazlali, I. Noshadi, Synthesis, rheological properties and magneto-viscos effect of Fe2O3/paraffin ferrofluids, J. Taiwan Inst. Chem. Eng. 43 (1) (2012) 159–164.
[21] S. Motahar, N. Nikkam, A.A. Alemrajabi, R. Khodabandeh, M.S. Toprak, M. Muhammed, Experimental investigation on thermal and rheological properties of n-octadecane with dispersed TiO_2 nanoparticles, Int. Commun. Heat Mass Transfer 59 (2014) 68–74.
[22] S. Motahar, N. Nikkam, A.A. Alemrajabi, R. Khodabandeh, M.S. Toprak, M. Muhammed, A novel phase change material containing mesoporous silica nanoparticles for thermal storage: a study on thermal conductivity and viscosity, Int. Commun. Heat Mass Transfer 56 (2014) 114–120.
[23] R. Prabakaran, J. Prasanna Naveen Kumar, D. Mohan Lal, C. Selvam, S. Harish, Constrained melting of graphene-based phase change nanocomposites inside a sphere, J. Therm. Anal. Calorim. (2019), https://doi.org/10.1007/s10973-019-08458-4.
[24] M. Sheikholeslami, K. Vajravelu, Nanofluid flow and heat transfer in a cavity with variable magnetic field, Appl. Math. Comput. 298 (2017) 272–282.
[25] M. Sheikholeslami, S. Mehryan, A. Shafee, M.A. Sheremet, Variable magnetic forces impact on magnetizable hybrid nanofluid heat transfer through a circular cavity, J. Mol. Liq. 277 (2019) 388–396.
[26] The finite element method for fluid dynamics, in: O.C. Zienkiewicz, R.L. Taylor, P. Nithiarasu (Eds.), The Finite Element Method for Fluid Dynamics, Seventh edition, Butterworth-Heinemann, Oxford, 2014(pp. iii).
[27] J.N. Reddy, An Introduction to the Finite Element Method, New York (1993).
[28] J.C. De Los Reyes, S. González Andrade, A combined BDF-semismooth Newton approach for time-dependent Bingham flow, Num. Methods Part. Diff. Eq. 28 (3) (2012) 834–860.
[29] M.H. Matin, W.A. Khan, Laminar natural convection of non-Newtonian power-law fluids between concentric circular cylinders, Int. Commun. Heat Mass Transfer 43 (2013) 112–121.
[30] C. Gau, R. Viskanta, Melting and solidification of a pure metal on a vertical wall, J. Heat Transf. 108 (1) (1986) 174–181.